Geophys. J. Int. (2002) **150,** 362–376

Co-seismic slip from the 1995 July 30 $M_w = 8.1$ Antofagasta, Chile, earthquake as constrained by InSAR and GPS observations

M. E. Pritchard,[1] M. Simons,[1] P. A. Rosen,[2] S. Hensley[2] and F. H. Webb[2]

[1] *Seismological Laboratory, Division of Geological and Planetary Sciences, California Institute of Technology,* 1200 *E. California Blvd* 252-21, *Pasadena,* CA 91125, *USA. E-mail: matt@gps.caltech.edu*

[2] *Jet Propulsion Laboratory, California Institute of Technology, Pasadena,* CA 91109, *USA*

Accepted 2001 November 27. Received 2001 October 5; in original form 2001 April 16

SUMMARY

We analyse radar interferometric and GPS observations of the displacement field from the 1995 July 30 $M_w = 8.1$ Antofagasta, Chile, earthquake and invert for the distribution of slip along the co-seismic fault plane. Using a fixed fault geometry, we compare the use of singular-value decomposition and constrained linear inversion to invert for the slip distribution and find that the latter approach is better resolved and more physically reasonable. Separate inversions using only GPS data, only InSAR data from descending orbits, and InSAR data from both ascending and descending orbits without the GPS data illustrate the complimentary nature of GPS and the presently available InSAR data. The GPS data resolve slip near GPS benchmarks well, while the InSAR provides greater spatial sampling. The combination of ascending and descending InSAR data contributes greatly to the ability of InSAR to resolve the slip model, thereby emphasizing the need to acquire this data for future earthquakes. The rake, distribution of slip and seismic moment of our preferred model are generally consistent with previous seismic and geodetic inversions, although significant differences do exist. GPS data projected in the radar line-of-sight (LOS) and corresponding InSAR pixels have a root mean square (rms) difference of about 3 cm. Comparison of our predictions of vertical displacement and observed uplift from corraline algae have an rms of 10 cm. Our inversion and previous results reveal that the location of slip might be influenced by the 1987 $M_w = 7.5$ event. Our analysis further reveals that the 1995 slip distribution was affected by a 1988 $M_w = 7.2$ event, and might have influenced a 1998 $M_w = 7.0$ earthquake that occurred downdip of the 1995 rupture. Our slip inversion reveals a potential change in mechanism in the southern portion of the rupture, consistent with seismic results. Predictions of the satellite LOS displacement from a seismic inversion and a joint seismic/GPS inversion do not compare favourably with the InSAR observations.

Key words: earthquakes, InSAR, inverse theory, northern Chile, subduction zone.

1 INTRODUCTION

A primary goal of earthquake geodesy is to invert observations of surface displacement for the distribution of slip along the fault plane (e.g. Segall & Harris 1987; Du *et al.* 1992; Sagiya & Thatcher 1999). However, there are both fundamental and practical limitations to resolving slip from subduction earthquakes. All geodetic observations are made tens of kilometres from the fault plane, and the largest surface deformation is off-shore and inaccessible to measurement (e.g. Sagiya & Thatcher 1999). Therefore, any estimation of the slip distribution must include an analysis of our ability to resolve this slip (e.g. Du *et al.* 1992; Árnadóttir & Segall 1994; Thatcher *et al.* 1997; Sagiya & Thatcher 1999). In practice, observations of surface deformation are rather sparse (for example, at GPS benchmarks or along levelling lines), fundamentally limiting the ability to well-resolve slip along the fault plane. Interferometric synthetic aperture radar (InSAR) has the potential to overcome the practical limitations of poor spatial sampling by densely and accurately measuring the surface deformation field (for an overview of InSAR methodology, see Massonnet & Feigl 1998; Rosen *et al.* 2000). The limitation of using only on-shore data is not eliminated by InSAR, but can be reduced by using tsunami waveform data (e.g. Satake 1993, not considered here). In this paper, we invert InSAR and GPS measurements to determine the slip distribution from the $M_w = 8.1$, 1995 July 30 Antofagasta, Chile earthquake (see Fig. 1).

2 PREVIOUS WORK

The 1995 July 30 $M_w = 8.1$ earthquake began at about 5:11 am (GMT) beneath the Mejillones Peninsula (Monfret *et al.* 1995, NEIC), and ruptured unilaterally to the southwest (Delouis *et al.*

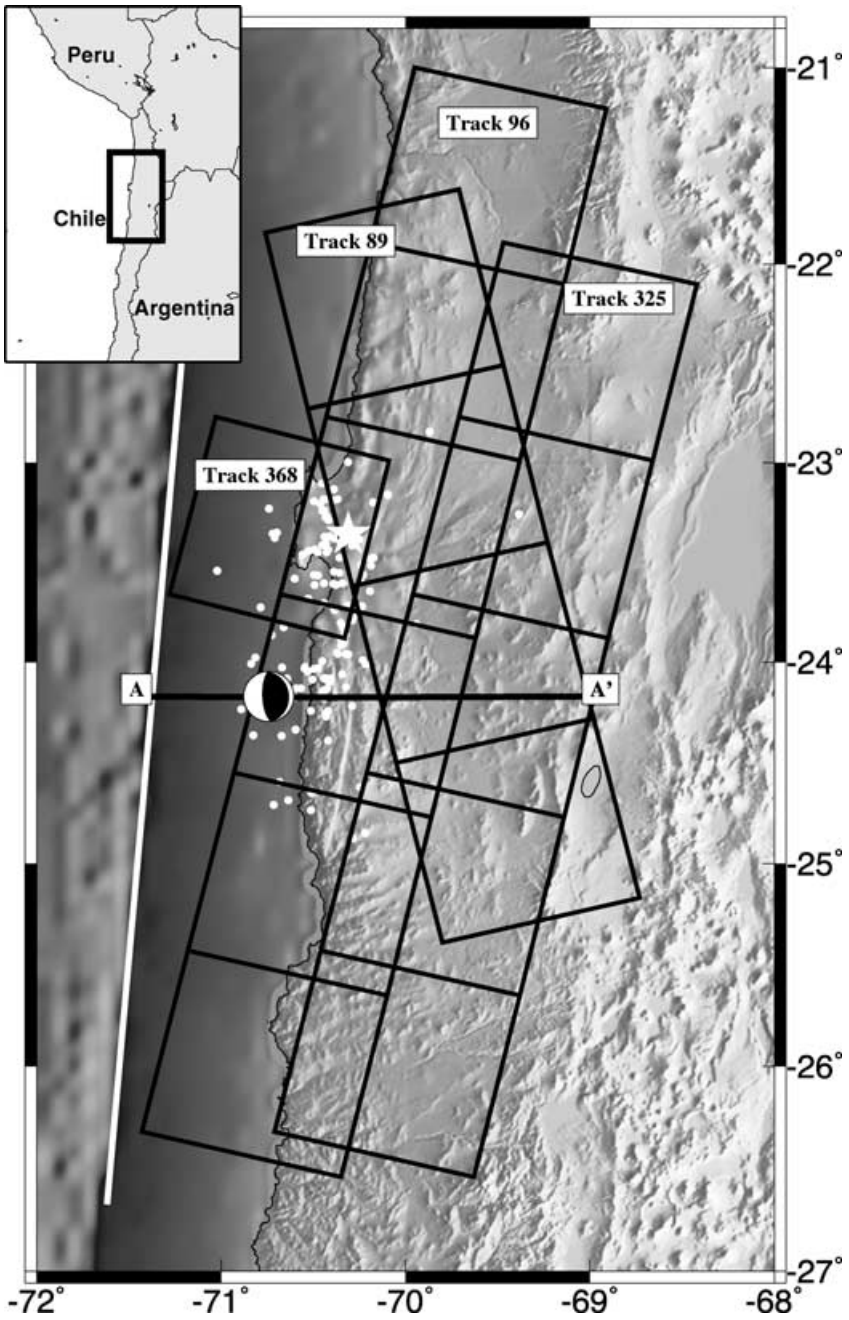

Figure 1. Reference map of our study area in northern Chile corresponding to the black box in the upper left-hand inset map. The Harvard CMT solution for the main shock is indicated, and the white star shows the location from the NEIC catalogue. Aftershocks with $M_w > 2.5$ are indicated by white dots (Husen *et al.* 1999). The white line indicates the surface trace of the fault along the subduction zone (at the bottom of the oceanic trench). Black squares outline the frames of ERS radar data used in this study. Profile A–A′ is shown in Fig. 5.

1997; Ihmlé & Ruegg 1997; Gouget *et al.* 1998; Carlo *et al.* 1999). A mild tsunami of 2.8 m beached in Antofagasta (Ramirez *et al.* 1997). The discrepancy between the moment magnitude, $M_w = 8.1$, and the surface wave magnitude, $M_s = 7.3$, is attributed to significant moment release at long periods and suggests that the event was a slow earthquake (Ruegg *et al.* 1996; Delouis *et al.* 1997; Carlo *et al.* 1999). The focal mechanism *p*-axis is nearly coincident with the plate convergence direction of NUVEL-1A (DeMets *et al.* 1994), and is inconsistent with significant slip partitioning at this location (Ruegg *et al.* 1996). Fig. 2 shows the relation between the 1995 earthquake and other large earthquakes in northern Chile.

Several studies consider both seismic and geodetic data from the earthquake (Ruegg *et al.* 1996; Delouis *et al.* 1997; Ihmlé & Ruegg 1997), although only Ihmlé & Ruegg (1997) did a joint seismic and geodetic inversion for fault slip. Delouis *et al.* (1997) found good agreement in a visual comparison between a finite fault model based on teleseismic body waves with observations made by Ortlieb *et al.* (1995) of coastal co-seismic uplift. Carlo *et al.* (1999) used teleseismic body and long-period surface waves to invert for the source time function. Reigber *et al.* (1997) published co-seismic interferograms of the 1995 earthquake covering a fraction of the deformation field near the Mejillones Peninsula. They found that

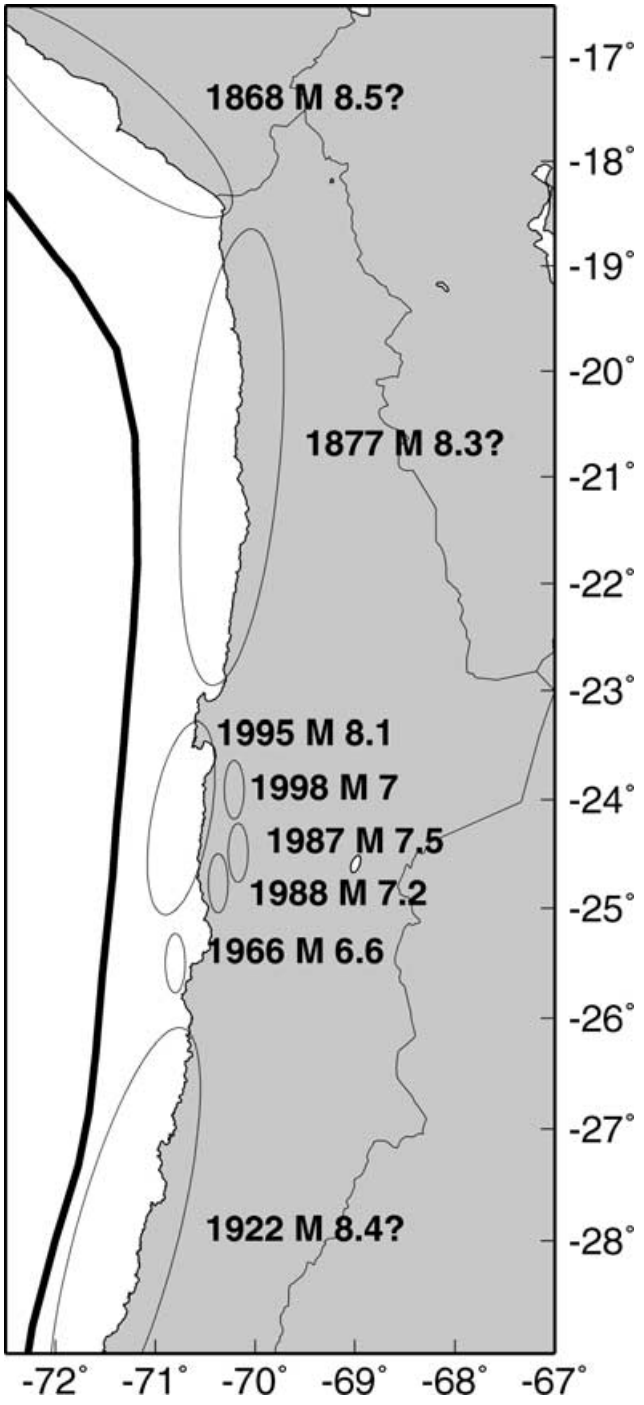

Figure 2. Estimated rupture zones for earthquakes in northern Chile with dates and approximate moments (Comte & Pardo 1991; Tichelaar & Ruff 1991; Ruegg *et al.* 1996; Delouis *et al.* 1997; Carlo *et al.* 1999). There is considerable uncertainty in the rupture areas for all but the 1995 event. In particular, the 1877 rupture zone could extend south into the 1995 rupture area (e.g. Lay *et al.* 1982).

the measured displacements were similar (a difference of less than 2 cm) to co-seismic vector displacements from seven GPS stations when projected in the radar line of sight (LOS). The GPS stations are part of the South American Geodynamic Activities (SAGA) project operated by the GeoForschungsZentrum Potsdam (GFZ). Klotz *et al.* (1999) used the co-seismic displacements from 70 GPS stations of the SAGA network to invert for the co-seismic slip distribution. Sobiesiak (2000) found a correlation between the *b*-value of the aftershock distribution from the 1995 earthquake and areas of high slip, perhaps providing a map of structural heterogeneities on the fault plane.

Although the Antofagasta earthquake has been extensively studied, several issues remain. Carlo *et al.* (1999) observed that there is no obvious relation between the distribution of co-seismic slip and the location of aftershocks, but suggested that a better-resolved 2-D slip map might reveal such a dependence. The primary goal of this study is a better-resolved 2-D slip map that can be used in future models of post-seismic deformation and to study interaction between the 1995 earthquake and events in 1987, 1988 and 1998. Ihmlé & Ruegg (1997) claimed that in order to fit the vertical component of GPS displacements, a change in dip of the subduction interface from 20° to 25° under the coast was required. Such a change in dip is not seen by other seismic studies (Delouis *et al.* 1996), although it is questionable whether the change in dip would be observed since it is below the resolution supported by those studies (Ihmlé & Ruegg 1997). A change in dip of the subduction interface was suggested by Armijo & Thiele (1990) as a possible cause of coastal uplift, and so another goal of this work is to determine whether the geodetic data require such a change in dip.

3 DATA USED

We use ERS-1 and ERS-2 radar images acquired between 1992 and 1997 (Fig. 1). We use radar data from four satellite tracks—three descending (tracks 96, 325 and 368) and one ascending (track 89). Radar interferometry measures the change in path-length in the radar LOS between observations. Data from the different viewing angles of the different satellite tracks provide multiple components of deformation. Interferograms include the effects of differences in satellite viewing geometry, topography, tropospheric and ionospheric changes, and deformation of the Earth's surface (e.g. Massonnet & Feigl 1998; Rosen *et al.* 2000). We process the SAR data using the Caltech/JPL repeat-orbit interferometry package, ROI_PAC (http://www-radar.jpl.nasa.gov/roi_pac/). In the processing, we use orbital information, accurate to about 20 cm, provided by the Delft Institute for Earth-Oriented Space Research in the Netherlands (Scharroo *et al.* 1998). We remove the topographic signal with both the two-pass approach where a pre-existing digital elevation model (DEM) is used, and the four-pass approach that uses ERS-1/2 tandem data (separated in time by 1 d). Existing DEMs in our study area have large gaps and poor accuracy in areas where they do exist. Therefore, we constructed a DEM of our area by mosaicking six pairs of tandem data from the four satellite tracks to use both in the two-pass approach and in the geocoding process. However, even our DEM has artefacts and cannot be used to remove topography when the perpendicular baseline is large, so for those interferograms we use the four-pass approach.

Northern Chile is an ideal location for the use of InSAR because the lack of rainfall, vegetation and human cultivation means that there is little non-tectonic change in the surface, even over long time periods. However, atmospheric variations can contaminate the deformation signal, especially near the coast. We minimize atmospheric contamination by using interferograms acquired on several different dates when atmospheric effects should be uncorrelated. From a geophysical perspective, northern Chile is a favourable study area because the coast is closer to the trench than in many other subduction zones, so that more of the deformation signal is on land. Furthermore, the Mejillones Peninsula protrudes trenchward and allows us to observe part of the co-seismic uplift.

We had to address a number of problems with the raw data that otherwise would have made it impossible to obtain acceptable slip distributions. First, some of the raw data were corrupted with missing lines or, less commonly, unnecessary lines were added that caused a loss of coherence in the interferograms (as demonstrated by horizontal streaks in Fig. 7 of Reigber *et al.* 1997). The line counter within the raw data itself is often insufficient to solve this problem, so we used the onboard clock information to find the missing lines. Unfortunately the clock records have insufficient temporal precision so that many lines have the same 'time'. Even with the corrupted data fixed, radar data were not collected during most passes over the area, so that all interferograms include deformation from multiple sources. Temporal coverage for the ascending track is especially poor. Only two ascending interferograms can be made that include co-seismic deformation, one of which has severe short-wavelength atmospheric or ionospheric distortion rendering it useless, and the other spans a time period of 4.5 yr. Even when the data were acquired, not all of the frames of a given satellite track were collected, so that maps of the deformation over some time intervals are shorter in along-track extent than others (Fig. 3). Additionally, we found that the pulse repetition frequency (PRF) can vary between acquisitions and that the baseline has a second-order variation that becomes important when many frames are concatenated. In the cases where precise ERS orbits were not available, we estimated the baseline directly from the data by removing a model of deformation and then finding the best-fitting orbital parameters that minimized the residual between the interferogram (with the model removed) and a synthetic interferogram made with a DEM (Rosen *et al.* 1996). To minimize possible short-wavelength atmospheric effects when estimating the baselines in this way, we use as many frames of radar data as possible in each satellite track (Fujiwara *et al.* 1998).

Fig. 3 shows four phase unwrapped interferograms with the observed LOS displacements, and Table 1 lists the nine interferograms we have used. The InSAR and GPS data contain several years of interseismic and several weeks to months of post-seismic deformation, although our examination of pre- and post-seismic images indicates that the co-seismic deformation makes up more than 90 per cent of the signal. For example, we see 15 fringes in the co-seismic interferograms and about one fringe in 2+ yr post-seismic interferograms (Pritchard *et al.*, in preparation). To remove possible interseismic and post-seismic deformation, we estimate the best-fitting quadratic ramps in space for each component of the displacement field (i.e. for each interferogram and each component of the GPS deformation) in addition to the fault slip model parameters. We have used a quadratic instead of a linear ramp to approximate the spatial shape of the interseismic strain that might decrease in a quasi-quadratic manner away from the trench (e.g. Savage 1983) and because InSAR orbital errors can also be quadratic in shape (e.g. Zebker *et al.* 1994).

Each of the satellite tracks used in this study has $O(10^8)$ pixels at full resolution, and even when transformed from radar to geographic coordinates using a low-resolution DEM there are $O(10^7)$ pixels. This number is currently impractical and as we will show, unnecessary for slip distribution inversion from large, relatively deep events. We use a uniform sampling by simply averaging nearby pixels together (commonly called 'looking down'), so that the total number of displacement measurements is manageable. Because the surface deformation pattern from the Antofagasta earthquake is smooth, averaging many pixels together does not lose any of the details of the deformation signal. This approach will fail in areas near where a fault ruptures the surface or the phase gradient is extremely high (such as at the Landers and Hector Mine, California earthquakes). To ensure that no information is lost by looking down the interferograms, we have estimated model parameters at different pixel resolutions and then computed the residual for all models at a high resolution (300 m pixels). Fig. 4 shows a comparison between the residuals from models calculated at 300 m pixel^{-1} and 2.5 km pixel^{-1}. The features in each residual are very similar and the rms residuals are within 0.6 cm. For the rest of the inversions discussed in this paper, we use the InSAR data with a spacing of 2.5 km, combined with the 65 GPS stations in the SAGA array (Klotz *et al.* 1999) totalling 5.6×10^4 observations.

4 DATA INVERSION

We fix the geometry of the fault plane using a quadratic function constrained by the location of the trench (from BOUND.90, compiled by Peter Sloss, unpublished) and the distribution of aftershocks (Husen *et al.* 1999). The surface is discretized into fault patches as shown in cross-section in Fig. 5 and map view in Fig. 6. The dip of our fault patches varies between 20° and 24°, consistent with the distribution of seismicity, 17°–18° (Comte *et al.* 1994; Delouis *et al.* 1996), calculations of the dip of the 1995 earthquake rupture plane, 15°–24° (Ruegg *et al.* 1996; Ortlieb *et al.* 1996; Delouis *et al.* 1997; Ihmlé & Ruegg 1997; Klotz *et al.* 1999; Carlo *et al.* 1999), and seismic refraction experiments, 9°–25° (Patzwahl *et al.* 1999). By fixing the geometry, the inversion for slip becomes linear and given by the equation $\mathbf{Gm} = \mathbf{d}$, where $\mathbf{m}$ is a vector of the strike-slip and dip-slip components of slip on each patch, $\mathbf{d}$ is the vector of displacement observations and $\mathbf{G}$ is the matrix of Green functions for each fault patch computed using an isotropic elastic half-space model (Okada 1985). We augment this linear system to include coefficients of a quadratic ramp in space for each component of GPS deformation and each interferogram. The fault patches are not all of the same size, and the size of each patch was selected to maximize the model resolution as discussed below. Each side of $\mathbf{Gm} = \mathbf{d}$ is multiplied by a weight matrix $P_{ij} = \delta_{ij}\sigma_j^{-1}$, where σ_j is the error on the ith datum (e.g. Harris & Segall 1987). We use the error on each component of the GPS measurements from Klotz *et al.* (1999). The errors on the InSAR measurements are not well-constrained, but we assume an uncorrelated error of 1 cm on each radar pixel in each track.

We compare the results from two methods: truncated singular-value decomposition (SVD) (e.g. Menke 1989; Press *et al.* 1994) and a least-squares constrained linear inversion (CLS). The constrained linear inversion (also called the iterative linear least-squares inversion) is part of the MATLAB Optimization Toolbox and is based on the work of Gill *et al.* (1981) and Coleman & Li (1996). We constrain the dip-slip component to only allow reverse faulting and the strike-slip component to be right-lateral, consistent with the plate convergence direction and previous estimates of the mechanism of the 1995 event. On the other hand, the SVD inversion is unconstrained, which will reduce the model resolution (e.g. Du *et al.* 1992). However, care must be taken when estimating the truncation value p, because of the well-known tradeoff between model variance and data misfit (e.g. Menke 1989). For the SVD inversion, model resolution is given by $R = V_p V_p'$, (e.g. Menke 1989), where V_p is the reduced set of model space eigenvectors. To determine the model resolution when using CLS, we generate synthetic data by putting a unit of slip on each component of slip on each fault patch one at a time, adding noise, and then inverting the synthetic data for the fault slip. The slip that the inversion places on each patch then corresponds to a row in the model resolution matrix (Du *et al.* 1992). The quadratic ramp components are constrained to have an effect of the order of a few centimetres across the scene.

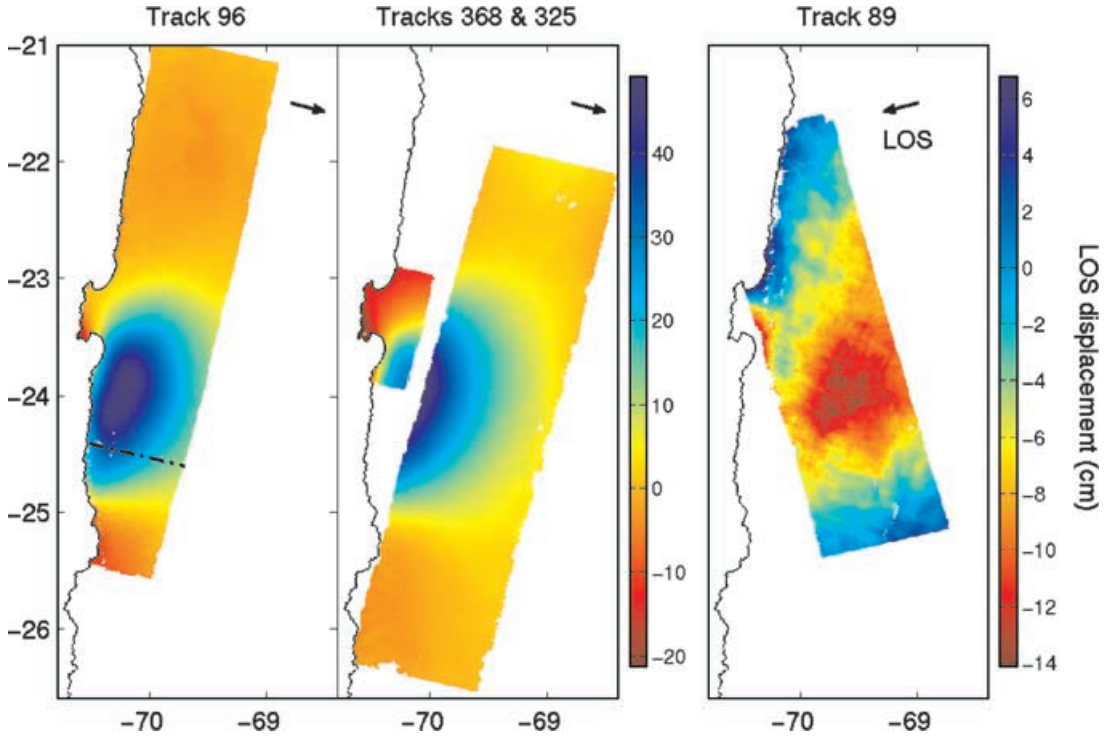

Figure 3. Unwrapped co-seismic interferograms used to invert for co-seismic slip from descending satellite tracks 96, 325, 368 and ascending track 89. The colour scale refers to change in the radar LOS direction in centimetres over the timescales indicated in Table 1. Black arrows show the LOS vector from the ground to the satellite projected on to the ground. We show the interferogram from track 96 spanning 1992 May 8 to 1995 October 9, because the other acquisitions do not span all available frames (the dotted black line shows where they end). For track 325, all interferograms have the same length and the interferogram spanning 1995 May 24 and 1995 September 19 is shown for reference. The maximum observed LOS displacement is about 50 cm away from the satellite in the descending scenes where there is co-seismic subsidence and westward horizontal displacement, both of which increase the LOS distance. The LOS displacements in the ascending interferogram are smaller (maximum of about 10 cm) since the westward horizontal motions correspond to a decrease in LOS distance while subsidence increases the LOS distance, thereby partially cancelling each other.

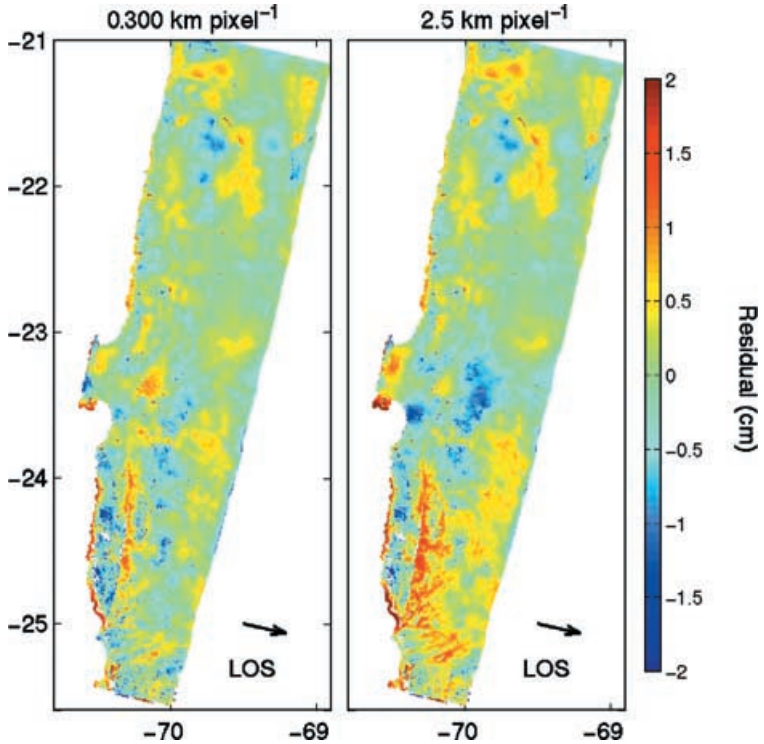

Figure 4. Residuals from models generated at different pixel spacings from track 96. The data used to calculate the residual is the same—0.300 km pixel^{-1}. The rms for model calculated at 2.5 km pixel^{-1} is 0.46 cm and for the model calculated 0.300 km pixel^{-1} is 0.40 cm.

Table 1. Data from three descending satellite tracks (96, 325 and 368) and one ascending track (89) used in inversions for co-seismic slip. $B_\perp$ refers to an estimate of the perpendicular baseline at the beginning of each track. For comparison, the GPS data were collected in October and November in both 1993 and 1995 (Klotz *et al.* 1999).

Track	Pre-seismic image	Post-seismic image	$B_\perp$ (m)	$B_\perp$ topo pair (m)
96	1992 May 5	1995 October 9	50	120
96	1995 April 16	1995 October 8	110	120
96	1995 April 16	1995 July 30	200	120
96	1995 April 16	1997 October 13	20	120
325	1992 May 24	1995 August 15	80	100
325	1992 May 24	1995 September 19	40	100
325	1995 July 11	1995 September 19	130	100
89	1993 May 28	1997 October 12	150	300
368	1995 July 14	1995 August 18	50	300

As mentioned above, because our geodetic data are limited to be on land, not all of the fault patches are equally well resolved. We define an effective resolution to be $\bar{R} = \sqrt{(R_d^2 + R_s^2)/2}$, where R_d is the dip-slip and R_s is the strike-slip diagonal component of the model resolution matrix. In an iterative, manual process, we adjust the size of each fault patch so that all of the patches have a CLS resolution above 0.8. The dip-slip component of a patch is generally better resolved than the strike-slip component, but for simplicity we keep strike-slip patches the same size as dip-slip patches. Our final parametrization has 41 patches (with two slip components per patch) with 72 parameters for the quadratic ramps (absolute phase offset, linear and quadratic spatial variations for each interferogram and component of GPS deformation), giving a total of 154 parameters. With more than 5.6×10^4 observations and judicious construction of spatially variable subfaults, the problem is no longer underdetermined. This variable patch size approach also provides an easy visual assessment of the spatially variable model resolution.

5 DISCUSSION

Fig. 6 shows a comparison between the model resolution and slip distribution from the CLS inversion and SVD inversions that are truncated at two different values. Our preferred SVD inversion uses the singular value ($p = 112$) above which the rms residual was rather constant (Sagiya & Thatcher 1999) (Fig. 7). The fact that we zero out less than one-third of the total of 154 parameters indicates that the majority of parameters are well-resolved (Segall & Harris 1987; Harris & Segall 1987). In general, the resolution from the constrained inversion is greater than for the unconstrained inversion (e.g. Du *et al.* 1992). It is not surprising that the CLS slip model is well-resolved since we use it to determine the fault size parametrization. The direction of slip in the CLS model is consistent from patch

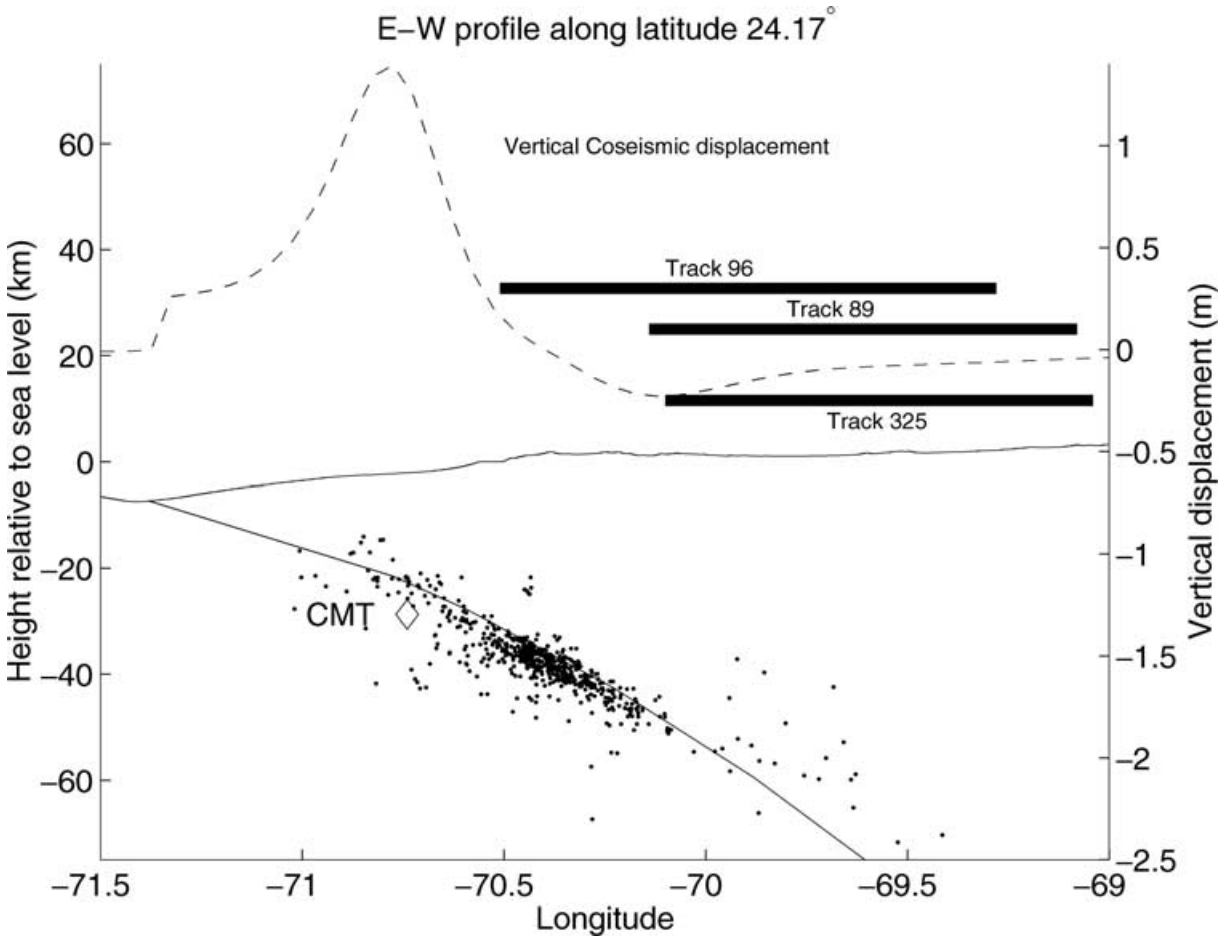

Figure 5. Profile along A–A′ from Fig. 1. The dashed line shows a profile of the vertical co-seismic displacement from our model prediction. The dots show all of the aftershocks taken from (Husen *et al.* 1999)—not just those along the profile. The black line shows the parametrization of the fault plane used in the co-seismic slip inversions. The horizontal thick black lines show the width of the satellite tracks along this profile. The nearly horizontal thin black line shows the topography in the ocean and on land. The Harvard CMT location is shown as a diamond labelled 'CMT'.

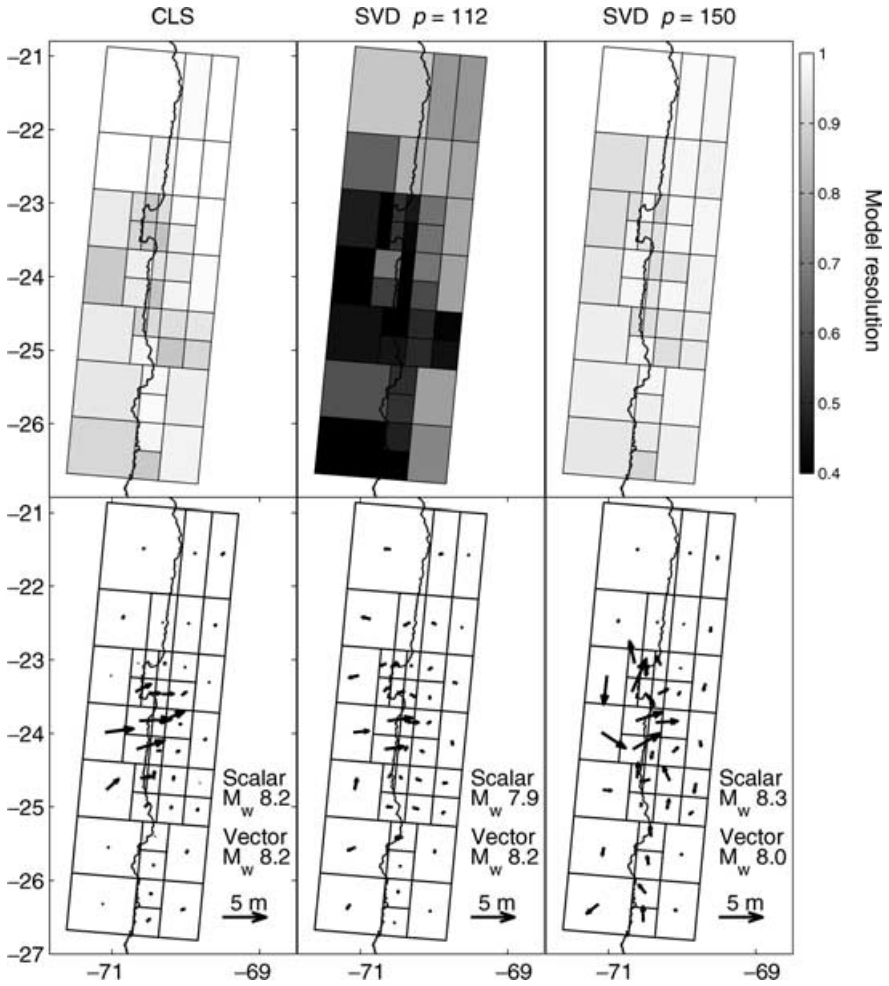

Figure 6. Comparison of model resolution and slip distribution from singular-value decomposition and constrained least-squares method. The patch size was determined to optimize CLS resolution (see the text for details). The model resolution and slip distribution for the SVD inversion depends on the number of singular values used. We prefer to truncate at 112 singular values, because keeping more singular values does not significantly reduce the rms residual, see Fig. 7. However, to more directly compare the SVD and CLS inversions, we also show results from an SVD inversion truncated at a singular value (150) that gives the same mean model resolution as the CLS inversion. The scalar and vector moments are shown for all inversions (see text).

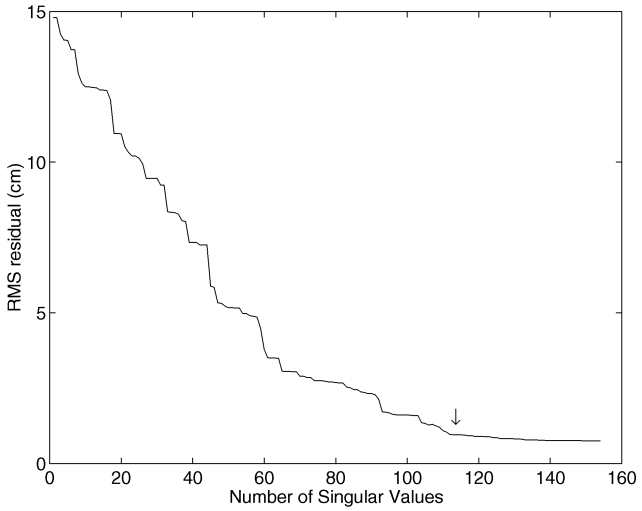

Figure 7. rms residual as a function of the singular value. We truncate singular values beyond 112 (arrow).

to patch and resembles the plate convergence direction and previous inversions of the 1995 mechanism. We find that the zone of aftershocks coincides well with the region of significant slip (Fig. 8), although, as others have observed, there are aftershocks but little slip in the northern half of the Mejillones Peninsula (e.g. Ruegg *et al.* 1996). The relatively poorer resolution of the SVD model ($p = 112$) allows some unlikely normal slip and slip well outside the 1995 rupture area. The SVD slip model would have higher resolution if more singular values are used (e.g. $p = 150$, Fig. 6). However, several model parameters in the inversion with 150 singular values are poorly determined, which means that some patches have an unrealistically large left-lateral slip. Alternatively, the resolution of the SVD model can be improved by changing the configuration of the fault patches and making some of them larger, but we instead choose to rely on the CLS inversion because it is better able to resolve the fine scale slip features. Fundamentally, the regularization provided by the SVD truncation does not allow for the geophysically reasonable *a priori* assumption of slip direction, while the CLS approach does. The rms residual from inversions using all the radar data and GPS for the SVD model ($p = 112$) is 0.96 cm, and for the CLS model

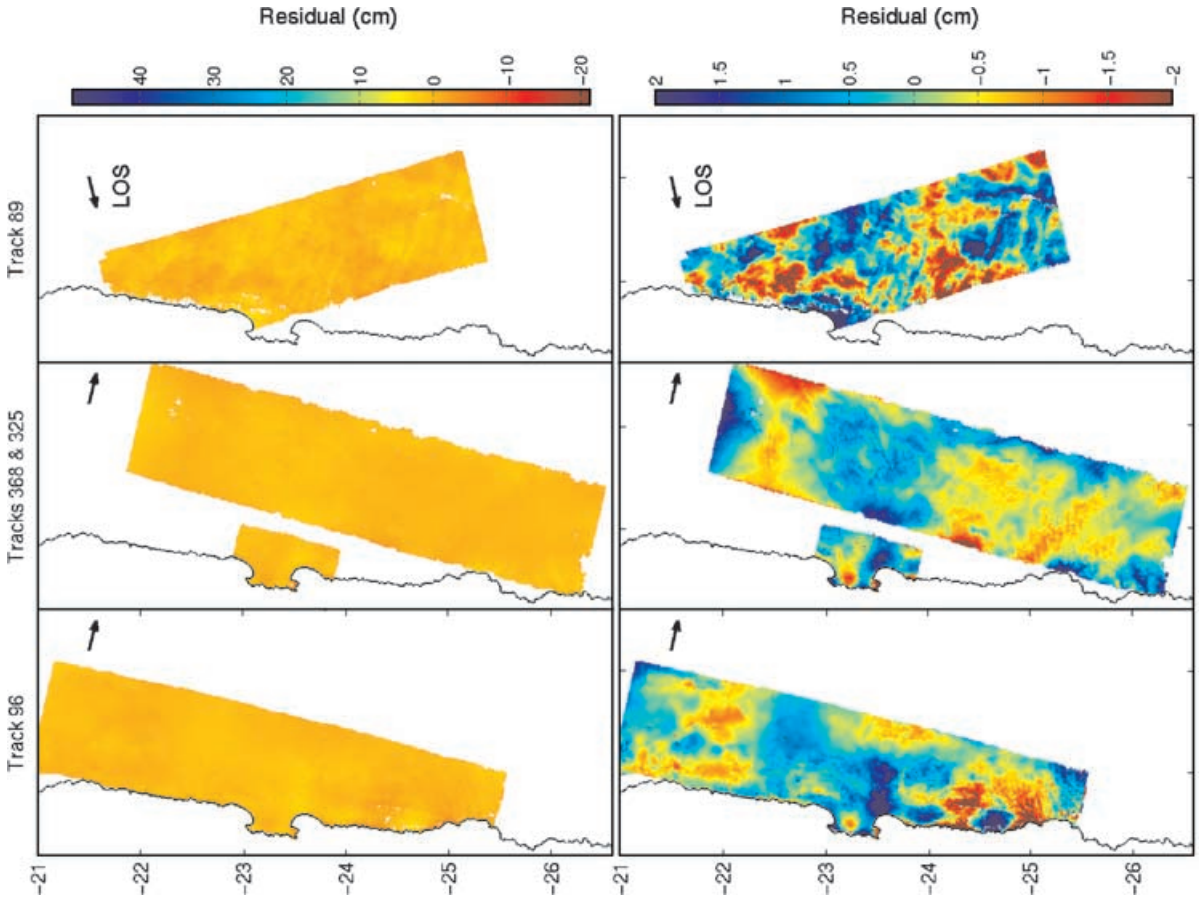

Figure 9. Residual of InSAR data from the preferred model for the four satellite tracks shown in Fig. 3. The colour scale used for displaying the data in Fig. 3 is shown in the top row and an expanded colour scale is used in the bottom row to show finer scale features. The rms residual from the four InSAR tracks shown are: 0.69 cm for track 96, 0.58 cm for track 325, 0.87 cm for track 368, and 1.0 cm for track 89.

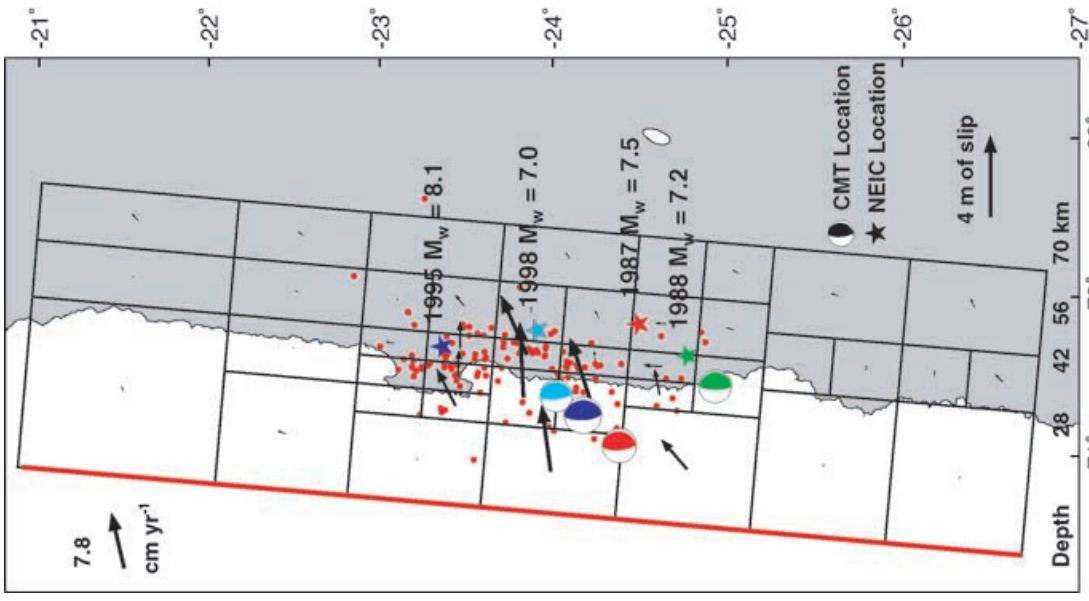

Figure 8. Preferred model of co-seismic slip from the 1995 earthquake constrained using GPS from Klotz *et al.* (1999) and three descending and one ascending tracks of radar data shown by the slip arrows of foot wall. The red dots are aftershocks with $M_w > 2.5$ from the 1995 event (Husen *et al.* 1999). The arrow in the upper left shows the magnitude and direction of the plate convergence rate (DeMets *et al.* 1994). The NEIC and Harvard CMT locations for the 1995 and three $M_w = 7$ events are shown as stars and moment tensors, respectively. (The NEIC location is where the earthquake began and the CMT location is the centre of moment release.) Reference depths along the parametrized fault plane are indicated at the bottom of the figure.

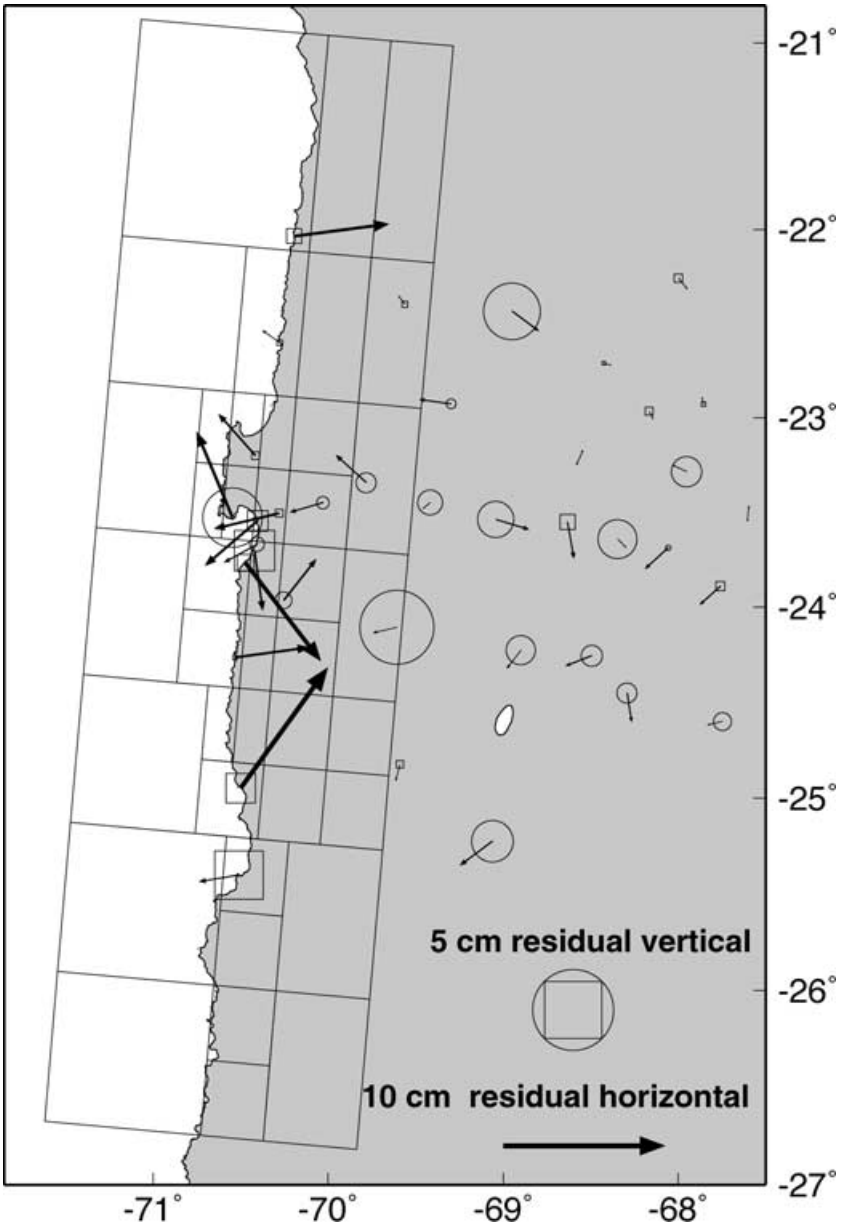

Figure 10. Residual displacements (data minus model) for the GPS data of Klotz *et al.* (1999). Horizontal residuals shown as arrows. Positive vertical residuals are circles and negative vertical residuals are squares. Using all stations, the rms for east, north, and up are: 1.8, 1.8 and 1.7 cm, respectively, and total rms for all components is 1.8 cm. If we consider only the 38 GPS stations shown in this figure the rms for east, north, and up are: 2.3, 2.2 and 1.9 cm, respectively, and total rms for all components is 2.1 cm.

is 0.80 cm. Fig. 9 shows the InSAR residual from the CLS model and Fig. 10 shows a comparison between the predicted and actual GPS displacements. While Ihmlé & Ruegg (1997) suggest that their GPS data set requires an abrupt change in slab dip, we find that the residual for the GPS data is effectively the same for models that assume a constant dip of the subduction zone fault (the results are not shown).

The geodetic moment from our preferred model is 2.4×10^{21} N m, equivalent to $M_w = 8.2$, and slightly larger than the other estimates (see below). However, a small portion of the slip may represent aseismic, interseismic or post-seismic slip that could not be fitted by our quadratic ramp. When we only consider the 12 patches with more than 0.5 m of slip, the moment is 1.6×10^{21} N m, equivalent to $M_w = 8.1$ (assuming $\mu = 3.2 \times 10^{10}$ Pa). For comparison, the moment from the SVD model ($p = 112$) is 2.9×10^{21} N m ($M_w = 8.2$), but is only 1×10^{21} N m ($M_w = 7.9$) for the same 12 'co-seismic' patches. The magnitude of slip for this SVD model is less than the CLS model, because of the greater degree of smoothing inherent in the SVD. The moment from the SVD model truncated at 150 is higher—4.1×10^{21} N m ($M_w = 8.3$) or 1.5×10^{21} N m ($M_w = 8.1$) for the same 12 patches. However, the slip distribution in both SVD models is oscillatory, so that when the vector sum of the slip is used in computing the moment for all patches ('Kostrov' summation, see Kostrov 1974), the moments are reduced to 8.4×10^{20} N m ($M_w = 7.9$) and 1.1×10^{21} ($M_w = 8.0$) N m for the SVD models with 112 and 150 singular values, respectively. The vector sum for the CLS model is only slightly changed to 2.2×10^{21} N m ($M_w = 8.2$).

5.1 Comparison of the slip model with previous work

Our preferred slip model is shown in Fig. 8 with aftershock locations and epicentres of $M_w = 7$ events that have ruptured near the main shock during the past 15 yr. The seismic moment from our CLS model, considering only the 12 patches with more than 0.5 m of slip (1.6×10^{21} N m), agrees well with other estimates: seismic 1.6×10^{21} N m (Carlo *et al.* 1999), 1.5×10^{21} N m (Gouget *et al.* 1998), 1.2×10^{21} N m (Delouis *et al.* 1997), 0.9×10^{21} N m (Ruegg *et al.* 1996); seismic and GPS 1.42×10^{21} N m (Ihmlé & Ruegg 1997); GPS 1.78×10^{21} N m (Klotz *et al.* 1999), 1.5×10^{21} N m (Ruegg *et al.* 1996); coralline algae 2×10^{21} N m (Ortlieb *et al.* 1996). Some of the spread in moment estimates can be explained by the different elastic structures used in the models (which vary from model to model by as much as 10 per cent). However, some have argued that the discrepancy between the seismic moment inferred from geodesy and long-period seismic waves is larger than body-wave-based estimates (e.g. Ruegg *et al.* 1996; Delouis *et al.* 1997), possibly indicating significant moment release at low frequencies (Ihmlé & Ruegg 1997; Carlo *et al.* 1999).

We estimate rakes for the fault patches with the best constrained slip to lie between 92° and 136° (with a mean of 113°) except for one patch (discussed below). Our estimated rake is close to the plate convergence direction of 103° (DeMets *et al.* 1994) and consistent with 97°–116° measured using a variety of techniques (Carlo *et al.* 1999; Ruegg *et al.* 1996; Delouis *et al.* 1997; Ihmlé & Ruegg 1997). The GPS-only inversion estimated the rake as 66° (Klotz *et al.* 1999), which is 114° using our convention for rake direction. One patch at the southeastern corner of the 1995 rupture area has a rake that is purely right-lateral. Delouis *et al.* (1997) fit a subevent with a normal mechanism late in the rupture and Carlo *et al.* (1999) noted that this part of the rupture is difficult to fit with a thrust mechanism. We constrain our patches to slip in only a reverse and right-lateral sense, so we cannot detect normal motion. The rake of this patch is very different from the others, indicating a possible local change in mechanism, but future joint geodetic and seismic inversions that allow for normal slip will be necessary to reconcile the data sets. This change in mechanism is spatially close to the location of a possible triggered shallow slip of the Atacama fault (Delouis *et al.* 1997; Klotz *et al.* 1999), but the observations of surface rupture are ambiguous (Ruegg *et al.* 1996; Ortlieb *et al.* 1996).

Carlo *et al.* (1999) conclude that the 1995 earthquake was very smooth with no certain 'asperities', but with three areas of enhanced moment release. Although our fault patches are large and do not resolve detailed structure, our slip distribution is relatively continuous and consistent with this result. We observe the maximum slip near the CMT location, as have others (Carlo *et al.* 1999; Delouis *et al.* 1997; Klotz *et al.* 1999), and the magnitude (4 m) is within a range of previous estimates—3.5 m (Klotz *et al.* 1999) and 10 m (Carlo *et al.* 1999). As with Ihmlé & Ruegg (1997), most of our slip is updip of the hypocentre and we do not have much slip between the hypocentre (NEIC location) and the CMT location (∼30 per cent), where the body-wave-only inversions put 80 per cent or more of the slip. Ihmlé & Ruegg (1997) attribute the difference in the location of moment release between the body wave and surface wave/geodetic studies to the fact that body-wave-only inversions do not approximate the rupture well.

The slip from the 1995 earthquake can be compared with the location of several $M_w = 7$ earthquakes that occurred within the rupture area. Near the hypocentre of the $M_w = 7.5$, 1987 earthquake, slip during the 1995 earthquake is primarily near the trench, while further north, slip is closer to land. The seismic moment also decreases from north to south. Furthermore, our slip distribution indicates that the 1995 event had little slip near the rupture area of the 1988 $M_w = 7.2$ earthquake. Ihmlé & Ruegg (1997) and Delouis *et al.* (1997) explain these observations as being caused by the prior release of slip from the 1987 event, which must have been concentrated near the hypocentre, since the Harvard CMT location lies well updip in an area of high slip during the 1995 event. Alternatively, the absence of slip near the locations of the 1987 and 1988 events could be a result of aseismic slip, or the slip deficit could be released in a future event (Carlo *et al.* 1999). A preliminary inversion of an interferogram from the $M_w = 7.0$ 1998 event indicates that most of its slip was in a region of low slip during the 1995 earthquake, and down-dip of an area of large slip in the 1995 event (Pritchard *et al.*, in preparation).

5.2 Comparison with other measurements

To understand how the different data sets used in the inversion contribute to the estimation and resolution of slip, we conduct three separate inversions: one with only GPS data, one with only InSAR data from descending orbits only and one with all available InSAR data. Not surprisingly, inversions with only GPS data best resolve the slip near where there are GPS benchmarks (Fig. 11, upper left). Predicted interferograms made with the GPS-only model are very different (tens of centimetres) from the observed LOS displacements in areas where there are no GPS benchmarks (Fig. 11). The model patches near the trench can cause more horizontal than vertical deformation on land, and because GPS data are more sensitive than InSAR to the horizontal component, the former better resolve slip near the trench. However, when both ascending and descending InSAR data are used, the model resolution near the trench is nearly the same as the GPS resolution of those patches, and illustrates the importance of acquiring both ascending and descending data.

Our resolution tests also show that addition of a single frame from track 368 and the addition of multiple interferograms spanning different time intervals also aid in model resolution, although the ascending track contributes the most. The combined GPS and InSAR resolution of these patches (Fig. 6) is higher than the resolution of either independent data set, as found for the 1992 Landers, California, strike-slip earthquake (Hernandez *et al.* 1999). The synergistic combination of GPS and InSAR becomes less important when we consider all possible InSAR data. We did not use the single frame of co-seismic data from the ascending track immediately south of track 89 in our inversions, but when we include synthetic data from this track in our SAR-only model resolution tests, the resolution is comparable with the combined InSAR/GPS resolution. This further illustrates the importance of collecting both ascending and descending orbits, and indicates that in some locations, remote sensing SAR data alone can resolve model parameters as well as data acquired on the ground with sparse GPS arrays.

The GPS and InSAR measurements of deformation can be directly compared when the GPS station lies within a part of the interferogram that was successfully unwrapped (Fig. 12). The GPS data were projected into the radar LOS and both the GPS and InSAR raw data were corrected by the best-fitting quadratic ramp calculated during the inversion of co-seismic slip. The quadratic ramp independently corrects for any potential interseismic slip in both the InSAR and GPS (because they span different time periods) and systematic InSAR orbital errors. The rms error for 90-point comparisons between InSAR and GPS in the nine interferograms is 3.2 cm, which is larger than the vertical GPS error of about 5 mm (Klotz *et al.* 1999), which dominates because of the steep

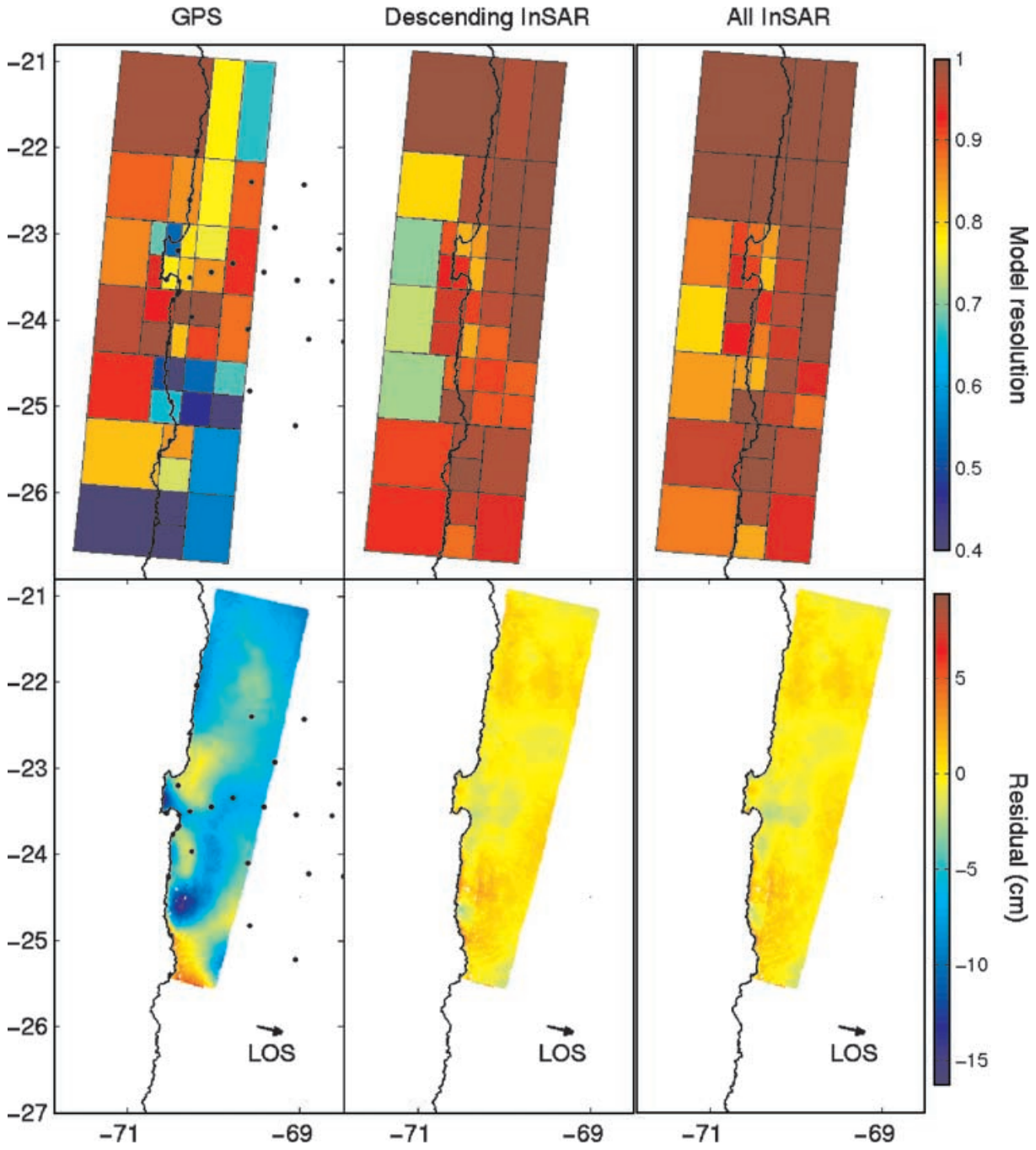

Figure 11. Comparison between model resolution and the difference between observed and predicted interferograms for inversions that used only the GPS data (top) only descending InSAR data (middle) and ascending and descending InSAR data (bottom). The residual from the interferogram spanning 1992 May 8 to 1995 October 9 from track 96 is shown, since this span includes the most GPS points and most closely matches the interval over which the GPS data were collected. The black dots on the two leftmost figures show the location of the GPS stations.

incidence angle, but is comparable with results at other earthquakes. The estimated 5 mm vertical error is probably optimistic for campaign GPS measurements. Published rms differences between InSAR and GPS measurements from the 1992 Landers, California earthquake are 3.4 cm for nine points (Massonnet *et al.* 1993), 11 cm for 19 points (Massonnet & Feigl 1998) and 18.9 cm for 18 points (Zebker *et al.* 1994), 1.6 cm for seven points for the 1994 Northridge, California, earthquake and about 1.0 cm for 34 points from the 1999 Hector Mine, California, earthquake (Simons & Fialko, personal communication).

We compare the uplift of coralline algae at 27 points along the coast measured by (Ortlieb *et al.* 1996), and revised by Ortlieb (personal communication, 2000), with the predicted uplift from our preferred model (Fig. 13). The rms difference is 10.9 cm. The largest discrepancy is at the point of maximum uplift (0.8 m), near Punta Tetas, where the predicted value more closely matches the preliminary estimate (Ortlieb *et al.* 1995) than the final one, although Ortlieb *et al.* (1996) discusses why the precision of this measurement might be poor. Ortlieb *et al.* (1996) states that some localized tectonic motion might be necessary to account for the observed

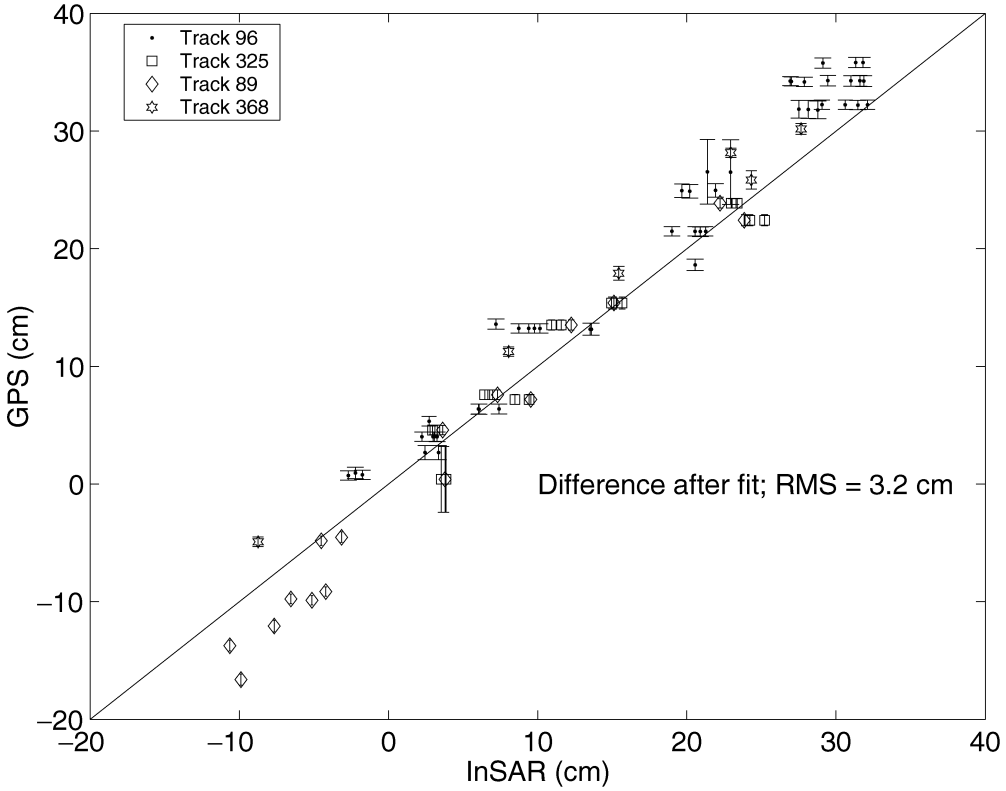

Figure 12. Comparison between 90 GPS displacements (Klotz *et al.* 1999) projected in the radar LOS and InSAR observations for the four satellite tracks. The independently determined best-fitting quadratic ramp from our preferred co-seismic model has been removed from the GPS and InSAR data. The rms difference is 3.2 cm.

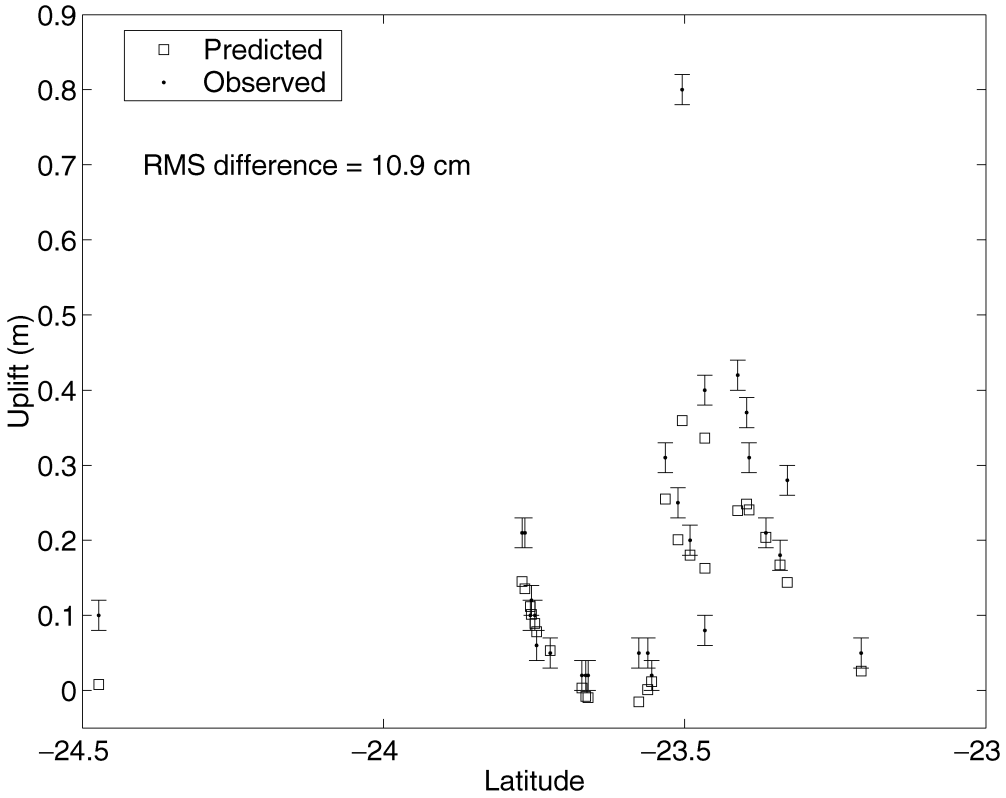

Figure 13. Comparison between our preferred co-seismic surface displacement model (squares) and the observed coast coralline algae uplift (dots) of Ortlieb *et al.* (1996), as revised by Ortlieb (personal communication, 2000). The rms difference is 10.9 cm, but if we remove the data point with the largest residual, the rms difference is 6.8 cm. Ortlieb *et al.* (1996) do not specify errors for each measurement, but estimate an overall precision of 2 cm, shown as the error bars.

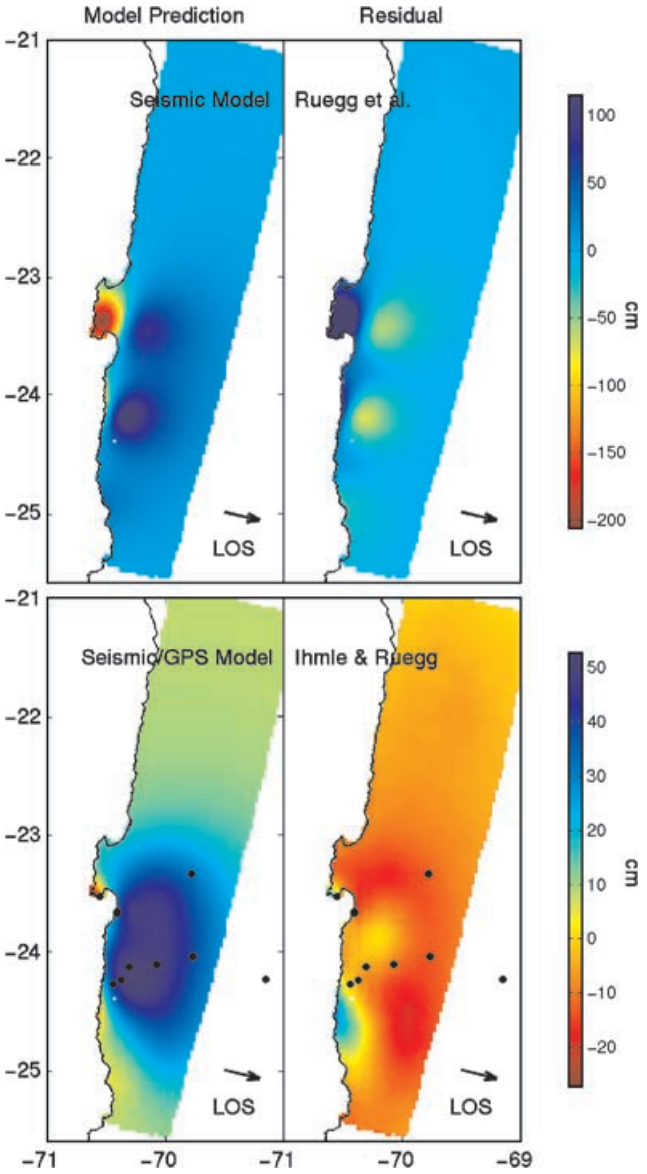

Figure 14. Predicted LOS displacements for track 96 from the models of Ruegg *et al.* (1996) (top left) and Ihmlé & Ruegg (1997) (bottom left) and the difference between the observations from the track 96 co-seismic pair and the prediction (top right and bottom right, respectively). The best-fitting quadratic ramp derived from our modelling was removed from the interferogram for the sake of comparison. The model of Ruegg *et al.* (1996) is a three point source model made from inversions of teleseismic body waves while the model of Ihmlé & Ruegg (1997) uses both teleseismic Rayleigh waves and 10 GPS stations (shown as black dots).

uplift at the southernmost point (Punta Tragagente), since there is no observed uplift along the coast to the immediate north or south. We do not see any evidence for such localized deformation in the interferograms, although such motion might be hard to detect, since in general, the correlation of the images decreases near the coast.

We compare the observed interferograms with those predicted from the models of Ruegg *et al.* (1996) and Ihmlé & Ruegg (1997) (Fig. 14). The model of Ruegg *et al.* (1996) is a three-point source model derived from inversions of teleseismic body waves, which explains the main features of the source time function, but poorly estimates the surface displacement. In particular, the region of uplift on the Mejillones Peninsula appears shifted to the north compared with our observations or the model of Ihmlé & Ruegg (1997). In a study of the induced tsunami, Guibourg *et al.* (1997) needed to shift the single patch of the Ruegg *et al.* (1996) displacement model to match the tide-gauge record at Antofagasta, but found that the variable slip model of Ihmlé & Ruegg (1997) adequately matches the gauge record. Ihmlé & Ruegg (1997) used both teleseismic Rayleigh waves and static displacements measured by 10 GPS stations to constrain the slip on the fault plane. The difference between their predicted LOS displacements and the observed interferogram are large (tens of centimetres) in places, although the difference is less near the locations of the GPS stations. Hernandez *et al.* (1997) compared synthetic interferograms generated with seismological models of slip from the 1992 Landers, California earthquake with observed interferograms. They found good agreement between the predicted and observed interferograms (centimetre-scale residual) except in regions within 7 km of the fault where they thought that the model fault parametrization might be too crude and the unwrapping of the observed interferogram might not be reliable. The fact that the seismic prediction at Landers more closely matches the observations than at Chile might be related to the fact that the Landers seismic inversion used local strong-motion data while the Chile seismic inversion relied upon teleseismic data.

6 SUMMARY

We have used two techniques to invert nine interferograms and GPS data spanning the 1995, $M_w = 8.1$ Antofagasta, Chile, earthquake for slip along the subduction zone interface. We favour the constrained least-squares inversion over the singular-value decomposition because CLS resolves model parameters and has a result that is more consistent (in terms of moment and rake) with previous geodetic and seismic inversions of slip. Our slip model shows an absence of slip near the location of several $M_w = 7$ earthquakes within the rupture area. Tests of the sensitivity to the inclusion of different subsets of the InSAR and GPS data demonstrate that the GPS data alone does not completely characterize surface deformation and that InSAR data from many different viewing geometries are necessary to maximize resolution. The difference between the GPS data projected into the radar LOS and the InSAR data are reasonable (about 3 cm) considering the long time periods spanned by both data sets and our simple removal of potential interand post-seismic deformation by fitting for quadratic ramps. The difference between our model of co-seismic uplift and observations of corraline algae uplift (Ortlieb *et al.* 1996) is 10 cm—we do not understand why this difference is so large. Predicted LOS displacements from seismic (Ruegg *et al.* 1996) and seismic/geodetic (Ihmlé & Ruegg 1997) models differ from observed interferograms by tens of centimetres. The discrepancy between the predicted LOS displacement from the model of Ihmlé & Ruegg (1997) and the observed interferograms is surprising considering the many similarities between their slip distribution and ours (see above). A complete joint InSAR/GPS/seismic inversion is necessary. A joint inversion will also test for a change in focal mechanism in the southeast portion of the rupture that we and others observe (Delouis *et al.* 1997; Carlo *et al.* 1999). As Carlo *et al.* (1999) and other have noted, there is no obvious relation between the distribution of aftershocks and slip. It might be that the aftershock distribution is more correlated to stresses induced by post-seismic than co-seismic deformation as is suggested for the 1994 Northridge earthquake (Deng *et al.* 1999). Post-seismic deformation is expected in the area since the co-seismic deformation is opposite long-term tectonic deformation in most places (Delouis *et al.* 1998), and is observed by GPS (Klotz *et al.* 2000).

ACKNOWLEDGMENTS

We acknowledge critical reviews from P. Segall and an anonymous reviewer. We are grateful to S. Husen, P. Ihmlé and L. Ortieb for access to their data, and thank D. Sandwell for suggesting using the satellite clock to help find missing lines. We thank E. Fielding for guidance in generating the DEM, made using ROI_PAC. The ERS SAR imagery has been acquired under research user category from Eurimage, Italy. GMT mapping software (Wessel & Smith 1998) was used to prepare figures. MEP was partly supported by an NSF Graduate Research Fellowship. Contribution number 8841 of the Division of Geological and Planetary Science, Seismological Laboratory, California Institute of Technology.

REFERENCES

Armijo, R. & Thiele, R., 1990. Active faulting in northern Chile: ramp stacking and lateral decoupling along a subduction plate boundary?, *Earth planet. Sci. Lett.,* **98,** 40–61.

Árnadóttir, T. & Segall, P., 1994. The 1989 Loma Prieta earthquake imaged from inversion of geodetic data, *J. geophys. Res.,* **99,** 21 835–21 855.

Carlo, D.L., Lay, T., Ammon, C.J. & Zhang, J., 1999. Rupture process of the 1995 Antofagasta subduction earthquake ($M_w = 8.1$), *Pure appl. Geophys.,* **154,** 677–709.

Coleman, T.F. & Li, Y., 1996. A reflective Newton method for minimizing a quadratic function subject to bounds on some of the variables, *SIAM J. Optimiz.,* **6,** 1040–1058.

Comte, D. & Pardo, M., 1991. Reappraisal of great historical earthquakes in the northern Chile and southern Peru seismic gaps, *Natural Hazards,* **4,** 23–44.

Comte, D., Pardo, M., Dorbath, L., Dorbath, C., Haessler, H., Rivera, L., Cisternas, A. & Ponce, L., 1994. Determination of seismogenic interplate contact zone and crustal seismicity around Antofagasta, northern Chile, *Geophys. J. Int.,* **116,** 553–561.

Delouis, B., Cisternas, A., Dorbath, L., Rivera, L. & Kausel, E., 1996. The Andean subduction zone between 22° and 25° (northern Chile): precise geometry and state of stress, *Tectonophysics,* **259,** 81–100.

Delouis, B. *et al.*, 1997. The $M_w = 8.0$ Antofagasta (Northern Chile) earthquake of 30 July 1995: a precursor to the end of the large 1877 gap, *Bull. seism. Soc. Am.,* **87,** 427–445.

Delouis, B., Phillip, H., Dorbath, L. & Cisternas, A., 1998. Recent crustal deformation in the Antofagasta region (northern Chile) and the subduction process, *Geophys. J. Int.,* **132,** 302–338.

DeMets, C., Gordon, R.G., Argus, D.F. & Stein, S., 1994. Effect of recent revisions to the geomagnetic reversal time scale on estimates of current plate motions, *Geophys. Res. Lett.,* **21,** 2191–2194.

Deng, J., Hudnut, K., Gurnis, M. & Hauksson, E., 1999. Stress loading from viscous flow in the lower crust and triggering of aftershocks following the 1994 Northridge, California, earthquake, *Geophys. Res. Lett.,* **26,** 3209–3212.

Du, Y., Aydin, A. & Segall, P., 1992. Comparison of various inversion techniques as applied to the determination of a geophysical deformation model for the 1983 Borah Peak earthquake, *Bull. seism. Soc. Am.,* **82,** 1840–1866.

Fujiwara, S., Rosen, P., Tobita, M. & Murakami, M., 1998. Crustal deformation measurements using repeat-pass JERS 1 synthetic aperture radar interferometry near the Izu Peninsula, Japan, *J. geophys. Res.,* **103,** 2411–2426.

Gill, P.E., Murray, W. & Wright, M.H., 1981. *Practical Optimization,* Academic Press, London.

Gouget, K., Ihmlé, P.F., Campos, J. & Montagner, J.-P., 1998. Self-consistent retrieval of source parameters using mantle waves, *Bull. seism. Soc. Am.,* **88,** 995–1002.

Guibourg, S., Heinrich, P. & Roche, R., 1997. Numerical modeling of the 1995 Chilean tsunami: impact on French Polynesia, *Geophys. Res. Lett.,* **24,** 775–778.

Harris, R.A. & Segall, P., 1987. Detection of a locked zone at depth on the Parkfield, California, segment of the San Andreas Fault, *J. geophys. Res.,* **92,** 7945–7962.

Hernandez, B., Cotton, F., Campillo, M. & Massonnet, D., 1997. A comparison between short term (co-seismic) and long term (one year) slip for the Landers earthquake: measurements from strong motion and SAR interferometry, *Geophys. Res. Lett.,* **24,** 1579–1582.

Hernandez, B., Cotton, F. & Campillo, M., 1999. Contribution of radar interferometry to a two-step inversion of the kinematic process of the 1992 Landers earthquake, *J. geophys. Res.,* **104,** 13 083–13 099.

Husen, S., Kissling, E., Flueh, E. & Asch, G., 1999. Accurate hypocentre determination in the seismogenic zone of the subducting Nazca Plate in northern Chile using a combined on-/offshore network, *Geophys. J. Int.,* **138,** 687–701.

Ihmlé, P.F. & Ruegg, J.-C., 1997. Source tomography by simulated annealing using broad-band surface waves and geodetic data: application to the $M_w = 8.1$ Chile 1995 event, *Geophys. J. Int.,* **131,** 146–158.

Klotz, J. *et al.*, 1999. GPS-derived deformation of the central Andes including the 1995 Antofagasta $M_w = 8.0$ earthquake, *Pure appl. Geophys.,* **154,** 709–730.

Klotz, J., Khazaradze, G., Cifuentes, O., Barriga, R., Barrientos, S., Perdomo, R., Viramonte, J. & Rios, V., 2000. The present-day kinematics of the central and southern Andes, *EOS,* **81,** 1126.

Kostrov, B.V., 1974. Seismic moment and energy of earthquakes, and seismic flow of rock, *Izv. Acad. Sci. USSR Phys. Solid Earth,* **1,** 23–40.

Lay, T., Kanamori, H. & Ruff, L., 1982. The asperity model and the nature of large subduction zone earthquakes, *Earthq. Predict. Res.,* **1,** 3–71.

Massonnet, D. & Feigl, K., 1998. Radar interferometry and its application to changes in the earth's surface, *Rev. Geophys.,* **36,** 441–500.

Massonnet, D., Rossi, M., Carmona, C., Adragna, F., Peltzer, G., Feigl, K. & Rabaute, T., 1993. The displacement field of the Landers earthquake mapped by radar interferometry, *Nature,* **364,** 138–142.

Menke, W., 1989. *Geophysical Data Analysis: Discrete Inverse Theory,* Academic Press, New York.

Monfret, T., Dorbath, L., Caminade, J.P., Pardo, M., Comte, D. & Ponce, L., 1995. The July 30, Antofagasta earthquake: an 'hypocritical' seismic event, *EOS, Trans. Am. geophys. Un.,* **76,** 427.

Okada, Y., 1985. Surface deformation to shear and tensile faults in a half space, *Bull. seism. Soc. Am.,* **75,** 1135–1154.

Ortlieb, L., Barrientos, S., Ruegg, J.C., Guzman, N. & Lavenu, A., 1995. Coseismic coastal uplift during the 1995 Antofagasta earthquake, in *IGCP Project 367: Late Quarternary Coastal Records of Rapid Change,* pp. 54–57, IInd Annual Meeting, Antofagasta, Chile, Abstract vol.

Ortlieb, L., Barrientos, S. & Guzman, N., 1996. Coseismic coastal uplift and coralline algae record in northern Chile: the 1995 Antofagasta earthquake case, *Quat. Sci. Rev.,* **15,** 949–960.

Patzwahl, R., Mechie, J., Schulze, A. & Giese, P., 1999. Two-dimensional velocity models of the Nazca plate subduction zone between 19.5°S and 25°S from wide-angle seismic measurements during the CINCA95 project, *J. geophys. Res.,* **104,** 7293–7317.

Press, W.H., Teukolsky, S.A., Vetterling, W.T. & Flannery, B.P., 1994. *Numerical Recipes in FORTRAN: the Art of Scientific Computing,* Cambridge University Press, New York.

Ramirez, J., Titichoca, H., Lander, J.F. & Whiteside, L.S., 1997. The minor destructive tsunami occurring near Antofagasta, Northern Chile, July 30, 1995, *Science of Tsunami Hazards,* **15,** 3–22.

Reigber, C., Michel, G.W., Klotz, J. & Angermann, D., 1997. The Antofagasta 1995 earthquake: crustal deformation pattern as observed by GPS and D-INSAR, in *Proc. ERS Symposium on Space at the Service of our Environment, Florence, Italy,* Vol. 414, pp. 507–513.

Rosen, P.A., Hensley, S., Zebker, H.A., Webb, F.H. & Fielding, E.J., 1996. Surface deformation and coherence measurements of Kilauea Volcano, Hawaii, from SIR-C radar interferometry, *J. geophys. Res.,* **101,** 23 109–23 125.

Rosen, P.A., Hensley, S., Joughin, I.R., Li, F.K., Madsen, S.N., Rodríguez, E. & Goldstein, R.M., 2000. Synthetic Aperture Radar Interferometry, *Proc. IEEE,* **88,** 333–382.

Ruegg, J.C. *et al.*, 1996. The $M_w = 8.1$ Antofagasta (North Chile) earthquake July 30, 1995: first results from teleseismic and geodetic data, *Geophys. Res. Lett.,* **23,** 917–920.

Sagiya, T. & Thatcher, W., 1999. Coseismic slip resolution along a plate boundary megathrust: the Nankai Trough, southwest Japan, *J. geophys. Res.,* **104,** 1111–1129.

Satake, K., 1993. Depth distribution of coseismic slip along the Nankai Trough, Japan, from joint inversion of geodetic and tsunami data, *J. geophys. Res.,* **98,** 4553–3565.

Savage, J.C., 1983. A dislocation model of strain accumulation and release at a subduction zone, *J. geophys. Res.,* **88,** 4984–4996.

Scharroo, R., Visser, P.N.A.M. & Mets, G.J., 1998. Precise orbit determination and gravity field improvement for the ERS satellites, *J. geophys. Res.,* **103,** 8113–8127.

Segall, P. & Harris, R., 1987. Earthquake deformation cycle on the San Andreas Fault near Parkfield, California, *J. geophys. Res.,* **92,** 10 511–10 525.

Sobiesiak, M.M., 2000. Fault plane structure of the Antofagasta, Chile earthquake of 1995, *Geophys. Res. Lett.,* **27,** 581–584.

Thatcher, W., Marshall, G. & Lisowski, 1997. Resolution of fault slip along the 470-km-long rupture of the great 1906 San Francisco earthquake, *J. geophys. Res.,* **102,** 5353–5367.

Tichelaar, B.W. & Ruff, L.J., 1991. Seismic coupling along the Chilean subduction zone, *J. geophys. Res.,* **96,** 11 997–12 022.

Wessel, P. & Smith, W.H.F., 1998. New, improved version of Generic Mapping Tools released, *EOS,* **79,** 579.

Zebker, H.A., Rosen, P.A., Goldstein, R.M., Gabriel, A. & Werner, C.L., 1994. On the derivation of coseismic displacement—fields using differential radar interferometry—the Landers earthquake, *J. geophys. Res.,* **99,** 19 617–19 634.